

Ultra broadband waveguide coupler using an anisotropic sub-wavelength metamaterial

Robert Halir^{1,2,*}, Pavel Cheben³, Jose Manuel Luque-González¹,
 Jose Darío Sarmiento-Merenguel¹, Jens Schmid³, Gonzalo Wangüemert-Pérez¹,
 Dan-Xia Xu³, Shurui Wang³, Alejandro Ortega-Moñux^{1,2}, and Íñigo Molina-Fernández^{1,2}

¹Universidad de Málaga, Dept. de Ingeniería de Comunicaciones, ETSI
 Telecomunicación, Campus de Teatinos s/n, 29071 Málaga, España

²Bionand Center for Nanomedicine and Biotechnology,
 Parque Tecnológico de Andalucía, 29590 Málaga, España

³National Research Council of Canada, Ottawa, Ontario, K1A 0R6, Canada

*Corresponding author: robert.halir@ic.uma.es

May 17, 2022

Multimode interference couplers are a fundamental building block in many integrated photonic systems, ranging from high-speed coherent receivers to quantum splitters [1, 2]. However, their basic structure has remained fundamentally unchanged for almost four decades [3], limiting their size and operation bandwidth [4]. Using sub-wavelength metamaterials, photonic devices with breakthrough size and performance have been recently reported [5–8]. Leveraging the inherent anisotropy of these structures, here we derive a semi-analytic expression that enables the design of compact and ultra broadband multimode interference couplers. We experimentally demonstrate virtually perfect operation over a bandwidth in excess of 300 nm (500 nm in simulation), for a device three times shorter than its conventional counterpart, making this the most broadband multimode interference coupler reported to date. These results will enable ultra broadband integrated systems for applications in communications and sensing [9, 10].

The self-imaging effect, by which a periodic optical field forms replicas of itself as it propagates, was described by Talbot in the early 19th century [11], and its application to integrated optics in the form of multimode interference couplers (MMIs) was first suggested 40 years ago [3]. MMIs are now fundamental building blocks in all integrated optical platforms, because of their ability to split and combine light with well defined amplitude and phase ratios [4]. They are used as key components in coherent optical receivers [1, 12], in the generation of indistinguishable photon pairs with quantum splitters [2], as ultralow-

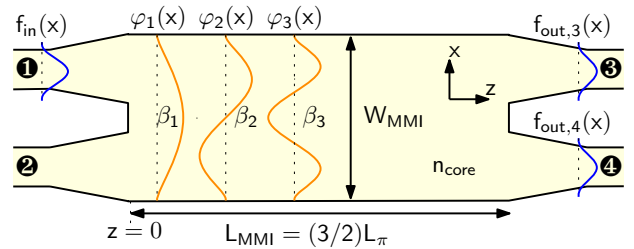


Figure 1: Schematic 2D model of a 2×2 MMI. When the mode of the input waveguide, $f_{in}(x)$, is launched into the multimode region it excites several higher modes, $\varphi_i(x)$, which interfere forming self-images of the input field. Coupling of these self-images to the output waveguide yields the output modes $f_{out,3}(x)$ and $f_{out,4}(x)$, each carrying exactly half of the input power, and a relative phase shift of 90° .

loss waveguide crossings for densely integrated optical circuits [13], or as on-chip mirrors [14, 15], to name but a few applications. At the same time, the principle of self-imaging in MMIs has been explored in a wide variety of materials, including non-linear media [16], dielectric loaded metals [17], hybrid plasmonic waveguides [18], and dielectric loaded graphene enabling wavelength tunability [19].

However, until very recently, the same classical MMI structure, shown in Fig. 1 for a 2×2 configuration, has been used. Consisting of an essentially rectangular central multimode region with tapered input and output waveguides, it provides a rugged design, but also imposes restrictions in terms of the size and bandwidth of these devices [4]. On the other hand, the recent advent of sub-wavelength structured waveguides (SWG), which suppress diffraction

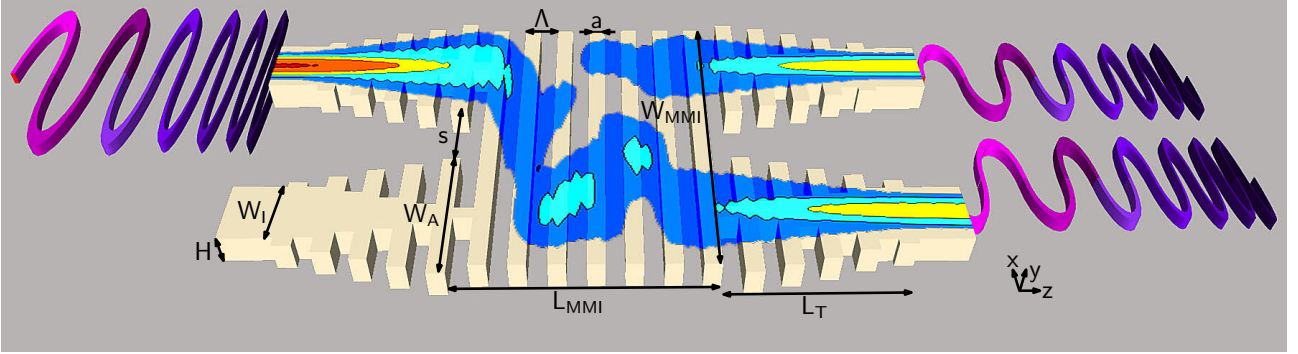


Figure 2: Ultra compact and broadband multimode interference coupler. The central multimode region is segmented at a sub-wavelength scale to engineer dispersion and anisotropy, achieving a beat-length that is virtually independent of wavelength. The SWG-taper input and output waveguides ensure efficient coupling to the silicon wire waveguides. In the illustration TE polarized light (polarized along x) with varying wavelength is injected into one of the input ports and is split among the two output waveguides with exactly the same amplitude and a 90° phase shift.

effects, has enabled the concept of refractive index engineering [5,6]. This concept has produced breakthrough devices for fiber-to-chip coupling [20, 21], wavelength demultiplexing [7], and polarization splitting [8], among other innovations. Applied to MMIs, sub-wavelength structures hold the potential to overcome the size and bandwidth limitations inherent to the classical MMI structure. Indeed, SWGs let to the first demonstration of a slotted MMI [22], which reduced the size of the device by a factor of two compared to a conventional MMI, without affecting its performance.

Building on a concept we introduced in [23], here we experimentally demonstrate, for the first time, a MMI that exploits the anisotropy and dispersion of a sub-wavelength metamaterial (see Fig. 2). Our fabricated device yields a three-fold size reduction compared to a conventional device, while at the same time achieving practically perfect performance (excess losses and imbalance < 1 dB, phase error $< 5^\circ$) over an unprecedented bandwidth of more than 300 nm around a central wavelength of $1.55 \mu\text{m}$. Full 3D simulations predict that bandwidths of ~ 500 nm are feasible; in simulation an optimized conventional MMI covers less than 200 nm with comparable performance. To the best of our knowledge this not only constitutes the MMI with broadest bandwidth ever demonstrated, but also one of the most broadband, fully passive integrated optical devices in general.

We first focus on the 2D model of the MMI shown in Fig. 1 in order to compare self-imaging in a conventional and a sub-wavelength patterned MMI. In both devices the mode field launched from the input waveguide, $f_{\text{in}}(x)$, is expanded into the modes of the multimode region, i.e. $f_{\text{in}}(x) = \sum_i c_i \varphi_i(x)$, with c_i the overlap between the input field and mode i . These modes propagate with different phase constants, β_i , producing self-images of the input field as they interfere. The distances at which these images form is

governed by the beat length of the two lowest order modes [4],

$$L_\pi = \frac{\pi}{\beta_1 - \beta_2}. \quad (1)$$

For instance, a double image of the input field is formed at $z = \frac{3}{2}L_\pi = L_{\text{MMI}}$, where L_{MMI} is the physical length of the multimode region (see Fig. 1). Since L_{MMI} is fixed, any wavelength variation of the beat-length will result in a detuning of the device and in a significant degradation of its performance.

In a conventional MMI, under the paraxial approximation, the beat length is given by

$$L_\pi^{\text{conv}} \approx \frac{4W_e^2}{3\lambda} n_{\text{core}}, \quad (2)$$

where n_{core} is the effective refractive index of the multimode region and λ is the free space wavelength as obtained with the effective index method. W_e is the effective width of the multimode region taking into account the Goos-Hähnchen shift, which is assumed to be the same for all modes and constant with wavelength [4]. The choice of the material platform clearly dictates the value of n_{core} and its wavelength dependence. The minimum width of the multimode region is determined by the separation (s) between the input/output waveguides, to avoid coupling between them, and the required width of the access waveguides (W_A), to control the excitation of higher order modes; see [12, 24] for details. Hence, there is little freedom to design the beat-length or its wavelength dependence.

Considering the $H = 220$ nm thick silicon platform with silicon dioxide (SiO_2) upper cladding, TE polarization, and the geometrical parameters given in table 1, Eq. (2) yields $L_\pi^{\text{conv}} \approx 27 \mu\text{m}$ at $\lambda = 1500$ nm. Figure 3 shows the beat-length calculated through Eq. (1), with $\beta_{1,2}$ obtained from a slab waveguide of width W_{MMI} , silicon-dioxide cladding, and n_{core} given by the effective index method. The beat-length

Table 1: **Geometrical parameters of the conventional MMI and the broadband MMI shown in Fig. 1 and 2.**

Parameter	Conv. MMI	SWG MMI
Silicon thickness (H)	220 nm	
Width MMI (W_{MMI})	3.25 μm	
Length MMI (L_{MMI})	38.5 μm	14 μm 74 periods
Width input (W_I)	0.5 μm	
Width access (W_A)	1.7 μm	
Length taper (L_T)	6 μm	5.7 μm 30 periods
separation (s)	0.3 μm	
Pitch (Λ)	-	190 nm
Duty-cycle (DC)	-	50 %
$n_{\text{core}} @ \lambda = 1500 \text{ nm}$	~ 2.87	$n_{xx} \sim 2.15$ $n_{zz} \sim 1.6$

is $L_{\pi}^{\text{conv}} \sim 28 \mu\text{m}$ at $\lambda = 1500 \text{ nm}$, in good agreement with Eq. (2). However, due to the strong wavelength dependence, the device will only operate in a limited bandwidth.

The fundamental advantage of our broadband MMI, shown in Fig. 2, arises from the inherent anisotropy of its sub-wavelength structure: two guided waves traveling in the central multimode region along the z and x directions “see” different structures [25]. Referring to the effective indexes of these waves as n_{xx} and n_{zz} , respectively, we see that in the 2D model shown in Fig. 1 the equivalent material in the multimode region can be described by the diagonal tensor $\mathbf{n}_{\text{core}} = \text{diag}[n_{xx}, n_{zz}]$. In such an anisotropic medium, the dispersion equation is given by $(k_x/n_{zz})^2 + (k_z/n_{xx})^2 = k_0^2$, where k_x is the wavevector in the x direction, $k_z = \beta$ is the propagation constant, and $k_0 = 2\pi/\lambda$ [26]. Using the procedure outlined in [4], we find that in this case the beat length is given by:

$$L_{\pi}^{\text{aniso}} \approx \frac{4W_e^2 n_{zz}^2}{3\lambda n_{xx}}. \quad (3)$$

The elements of effective index tensor can be calculated from the structure in the inset of Fig. 3: n_{xx} is the effective index of the fundamental Bloch mode traveling in the z direction and polarized along the x axis; n_{zz} is the effective index of the fundamental Bloch mode traveling in the x direction and polarized along the z axis. For the dimensions given in table 1, we find $n_{xx} \sim 2.15$, $n_{zz} \sim 1.6$ at $\lambda = 1500 \text{ nm}$. Equation (3) then predicts a significantly reduced beat length of $L_{\pi}^{\text{aniso}} \approx 11.5 \mu\text{m}$. Figure 3 shows the beat length calculated through Eq. (1), with $\beta_{1,2}$ obtained from an anisotropic slab waveguide of width W_{MMI} , silicon-dioxide cladding, and $\mathbf{n}_{\text{core}} = \text{diag}[n_{xx}, n_{zz}]$ [26]. From the figure, we find $L_{\pi}^{\text{aniso}} \sim 12 \mu\text{m}$ at $\lambda = 1500 \text{ nm}$, in good agreement with Eq. (3). More importantly we observe

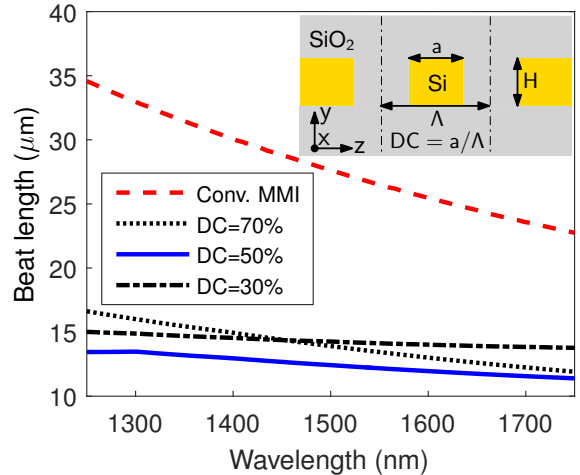


Figure 3: Semi-analytic calculation of the beat-length of a conventional MMI and the sub-wavelength patterned MMI modeled through an anisotropic medium. The anisotropy of the sub-wavelength MMI yields an almost three-fold reduction in beat-length compared to the conventional MMI, and, more importantly, virtually eliminates the wavelength dependence. The pitch is fixed at $\Lambda = 210 \text{ nm}$, while all other geometric parameters are given in table 1. The values of n_{xx} and n_{zz} are obtained through modal analysis from the structure shown in the inset.

that the beat-length becomes virtually flat with wavelength for the pitch of $\Lambda = 210 \text{ nm}$ considered here, and that the minimum beat length is achieved for a duty-cycle of 50%.

We use full 3D simulations to validate the predictions of our semi-analytic 2D model and assess the actual performance of both the conventional and the sub-wavelength patterned MMI. Fig. 4 shows the simulated wavelength dependence of the beat length of a conventional MMI; the propagation constants $\beta_{1,2}$ were obtained with a commercial mode solver [27]. As expected the beat length exhibits a strong variation, between 35 μm and 23 μm , resulting in de-tuning of the device when it is not operated at its design wavelength. For a conventional MMI with the optimized dimensions shown in table 1, the simulated impact of this de-tuning is shown Fig. 5, in terms of excess losses (EL), imbalance (IB) and phase error (PE). By denoting the complex transmission from the fundamental mode of (input) waveguide 1 to the fundamental mode of the (output) waveguides 3 and 4 by s_{31} and s_{41} [see Fig. 1], these performance parameters are: $\text{EL} = 10 \log(|s_{31}|^2 + |s_{41}|^2)$, $\text{IB} = 10 \log(|s_{31}|^2/|s_{41}|^2)$, and $\text{PE} = \angle(s_{31}/s_{41})$. From Figs. 5(a)-(c) it is clear that as the device is operated further away from its design wavelength its performance steadily deteriorates. Aiming for excess losses and imbalance below 1 dB and phase error smaller than 5° thus yields a bandwidth of just under 200 nm for this optimized simulated MMI.

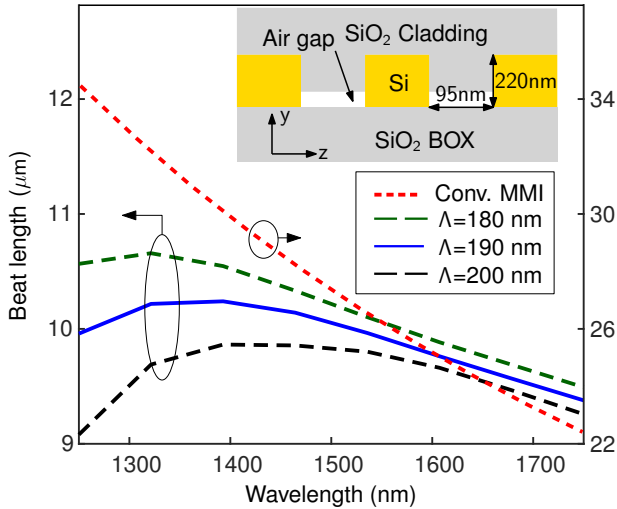


Figure 4: Full vectorial 3D simulations of beat length as a function of wavelength for a conventional MMI (right scale) and the wide-band MMI (left scale). With a judiciously designed pitch the SWG structure in the wideband MMI yields a much shorter and less wavelength dependent beat length. Inset: Schematic side-view of the SWG in the wideband MMI showing small air gaps under the SiO₂ upper cladding. The geometric parameters of the device are given in table 1.

The wavelength dependence of the beat-length in our sub-wavelength patterned MMI (see Fig. 2) is shown, for a 50% duty-cycle, in Fig. 4; the propagation constants $\beta_{1,2}$ were obtained using 3D-FDTD [28], and the procedure outlined in [29]. For the dimensions given in table 1, a pitch between 190 nm and 200 nm yields a virtually wavelength independent beat length in the 1250 nm to 1750 nm wavelength range. On the other hand, the beat length at $\lambda = 1500$ nm is $L_{\pi}^{\text{SWG}} \sim 10 \mu\text{m}$, which is a three-fold reduction compared to the conventional device. The inset of Fig. 4 illustrates the longitudinal cross-section of the MMI. In our initial design we assumed that the upper SiO₂ would completely fill the trenches between the silicon segments. However, our experimental results suggest that that is not the case, and that in fact an air gap of approximately 60 nm is left, due to the relatively high (2.3 : 1) high aspect ratio of the trenches. All simulation results presented from here on include this gap.

For a pitch of $\Lambda = 190$ nm the wavelength average beat length is $L_{\pi} \approx 10 \mu\text{m}$, yielding an approximate device length of $(3/2)L_{\pi}/\Lambda = 79$ periods for a 2×2 general interference MMI. We optimized the length of the device using 3D-FDTD simulations that take into account material dispersion. Device performance for the optimized length of 74 periods is shown in Fig. 5. These results confirm virtually perfect device operation over a 500 nm wavelength span, with excess losses and imbalance below 1 dB, and phase error below 5°.

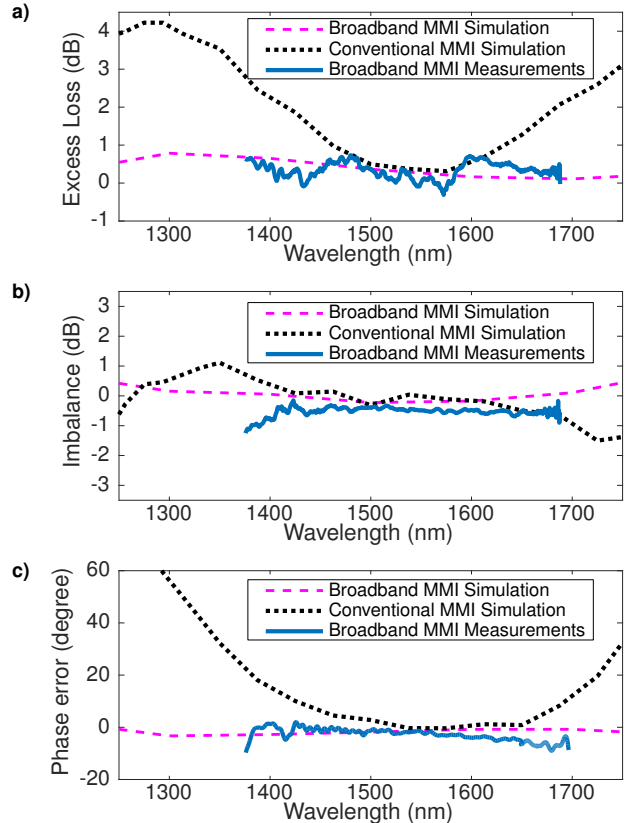


Figure 5: Measured and simulated performance of the wideband MMI compared to simulations of an optimized conventional MMI. a) Excess loss, b) Imbalance and c) phase error. The measurements of the wideband MMI reveal virtually perfect performance over more than 300 nm, while the (simulated) conventional MMI covers just under 200 nm while being three times longer.

This is an almost three fold bandwidth enhancement compared to the conventional MMI.

In order to experimentally validate the broadband operation of our device, we fabricated a chip containing both individual MMIs, asymmetric Mach-Zehnder interferometers and reference waveguides. To enable broadband light coupling to the chip we used sub-wavelength engineered fiber-to-chip mode transformers [20]. The devices were defined with electron beam lithography and transferred to the silicon layer with reactive ion etching. The SiO₂ upper cladding was deposited using plasma-enhanced chemical vapor deposition. Fig. 6 shows a SEM of one of the fabricated devices prior to the deposition of the SiO₂ upper cladding. Measurements were performed with two independent setups. An initial screening of the devices was performed using a tunable laser source at the input and power-detector at the output, covering the 1400 nm to 1600 nm range. In order to measure in an even broader range, we used a second setup with a broadband light source as input and an optical spectrum analyzer at the output. In both cases

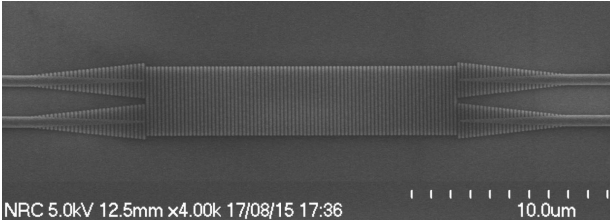


Figure 6: Scanning electron microscope image of one of the fabricated ultra broadband MMIs, prior to the deposition of the upper SiO₂ cladding.

the input polarization was set to quasi-TE (horizontal) using a polarization controller. To obtain excess losses, the transmission through an individual MMI is normalized to the transmission through a reference waveguide. The phase error is obtained from the interferogram that results from the asymmetric Mach-Zehnder interferometers, using a minimum-phase technique [30]. The measurement data from both setups were found to be in very good agreement in the common measurement range, with a deviation below 5° in phase, 0.5 dB in imbalance and 1 dB in excess loss. Fig. 5 shows the measurement results between 1375 nm to 1700 nm, revealing virtually perfect device performance, and confirming the wide-band behavior of the device. We observed a resonant behavior around 1350 nm, which is attributed to the increased duty cycle of the fabricated devices and could be addressed with proper pre-scaling of mask. Our broadband source does not extend beyond 1700 nm preventing measurements at longer wavelengths.

In conclusion, we have shown that the intrinsic anisotropy of sub-wavelength metamaterials can be exploited to design compact and ultra broadband multimode interference couplers. We have experimentally demonstrated couplers with virtually ideal performance over a 300 nm bandwidth, outperforming simulated conventional MMIs by a wide margin, and having the potential to achieve bandwidths of ~ 500 nm. We believe that these ultra broadband devices can usher in broadband integrated systems with applications in communications and sensing.

We acknowledge funding from the Ministerio de Economía y Competitividad, Programa Estatal de Investigación, Desarrollo e Innovación Orientada a los Retos de la Sociedad (cofinanciado FEDER), Proyecto TEC2013-46917-C2-1-R. We would like to thank Jean Lapointe for preparing files for e-beam lithography.

References

[1] P. Dong, X. Liu, S. Chandrasekhar, L. L. Buhl, R. Aroca, and Y.-K. Chen, “Monolithic silicon photonic integrated circuits for compact 100 gb/s coherent optical receivers and transmit-

ters,” *IEEE J. Sel. Top. Quantum Electron.* **20**, 150–157 (2014).

- [2] J. He, B. A. Bell, A. Casas-Bedoya, Y. Zhang, A. S. Clark, C. Xiong, and B. J. Eggleton, “Ultra-compact quantum splitter of degenerate photon pairs,” *Optica* **2**, 779–782 (2015).
- [3] R. Ulrich and G. Ankele, “Self-imaging in homogeneous planar optical waveguides,” *Appl. Phys. Lett.* **27**, 337–339 (1975).
- [4] L. B. Soldano and E. Pennings, “Optical multimode interference devices based on self-imaging: principles and applications,” *J. Lightwave Technol.* **13**, 615–627 (1995).
- [5] P. Cheben, P. J. Bock, J. H. Schmid, J. Lapointe, S. Janz, D.-X. Xu, A. Densmore, A. Delage, B. Lamontagne, and T. J. Hall, “Refractive index engineering with subwavelength gratings for efficient microphotonic couplers and planar waveguide multiplexers,” *Opt. Lett.* **35**, 2526–2528 (2010).
- [6] R. Halir, P. J. Bock, P. Cheben, A. Ortega-Moñux, C. Alonso-Ramos, J. H. Schmid, J. Lapointe, D.-X. Xu, J. G. Wangüemert-Pérez, Í. Molina-Fernández *et al.*, “Waveguide sub-wavelength structures: a review of principles and applications,” *Laser Photonics Rev.* **9**, 25–49 (2015).
- [7] A. Y. Piggott, J. Lu, K. G. Lagoudakis, J. Petykiewicz, T. M. Babinec, and J. Vučković, “Inverse design and demonstration of a compact and broadband on-chip wavelength demultiplexer,” *Nat. Photonics* **9**, 374–377 (2015).
- [8] B. Shen, P. Wang, R. Polson, and R. Menon, “An integrated-nanophotonics polarization beam-splitter with $2.4 \times 2.4 \mu\text{m}^2$ footprint,” *Nat. Photonics* **9**, 378–382 (2015).
- [9] A. Sano, T. Kobayashi, S. Yamanaka, A. Matsuura, H. Kawakami, Y. Miyamoto, K. Ishihara, and H. Masuda, “102.3-tb/s (224 x 548-gb/s) c- and extended l-band all-raman transmission over 240 km using pdm-64qam single carrier fdm with digital pilot tone,” in “National Fiber Optic Engineers Conference,” (Optical Society of America, 2012), pp. PDP5C-3.
- [10] D. Rodrigo, O. Limaj, D. Janner, D. Etezadi, F. J. G. de Abajo, V. Pruneri, and H. Altug, “Mid-infrared plasmonic biosensing with graphene,” *Science* **349**, 165–168 (2015).
- [11] H. F. Talbot, “Facts relating to optical science,” *Philos. Mag.* **9**, 401–407 (1836).

- [12] R. Halir, G. Roelkens, A. O.-M. nux, and J. G. Wangüemert-Pérez, “High-performance 90° hybrid based on a silicon-on-insulator multimode interference coupler,” *Opt. Lett.* **36**, 178–180 (2011).
- [13] Y. Zhang, A. Hosseini, X. Xu, D. Kwong, and R. T. Chen, “Ultralow-loss silicon waveguide crossing using bloch modes in index-engineered cascaded multimode-interference couplers,” *Opt. Lett.* **38**, 3608–3611 (2013).
- [14] E. Kleijn, M. Smit, and X. Leijtens, “Multimode interference reflectors: A new class of components for photonic integrated circuits,” *J. Lightwave Technol.* **31**, 3055–3063 (2013).
- [15] J. S. Fandiño, J. D. Doménech, and P. Muñoz, “Two-port multimode interference reflectors based on aluminium mirrors in a thick soi platform,” *Opt. Express* **23**, 20219–20233 (2015).
- [16] M. Tajaldini and M. Jafri, “Simulation of an ultra-compact multimode interference power splitter based on kerr nonlinear effect,” *Lightwave Technology, Journal of* **32**, 1282–1289 (2014).
- [17] Z. Zhu, C. E. Garcia-Ortiz, Z. Han, I. P. Radko, and S. I. Bozhevolnyi, “Compact and broadband directional coupling and demultiplexing in dielectric-loaded surface plasmon polariton waveguides based on the multimode interference effect,” *Appl. Phys. Lett.* **103**, 061108 (2013).
- [18] X. Guan, H. Wu, Y. Shi, and D. Dai, “Extremely small polarization beam splitter based on a multimode interference coupler with a silicon hybrid plasmonic waveguide,” *Opt. Lett.* **39**, 259–262 (2014).
- [19] R. Zheng, D. Gao, and J. Dong, “Ultra-compact broadband tunable graphene plasmonic multimode interferometer,” *IEEE Photonic Tech. L.* **28**, 645 – 648 (2016).
- [20] P. Cheben, J. H. Schmid, S. Wang, D.-X. Xu, M. Vachon, S. Janz, J. Lapointe, Y. Painchaud, and M.-J. Picard, “Broadband polarization independent nanophotonic coupler for silicon waveguides with ultra-high efficiency,” *Opt. Express* **23**, 22553–22563 (2015).
- [21] D. Benedikovic, P. Cheben, J. H. Schmid, D.-X. Xu, B. Lamontagne, S. Wang, J. Lapointe, R. Halir, A. O.-M. nux, S. Janz, and M. Dado, “Subwavelength index engineered surface grating coupler with sub-decibel efficiency for 220-nm silicon-on-insulator waveguides,” *Opt. Express* **23**, 22628–22635 (2015).
- [22] A. Ortega-Moñux, C. Alonso-Ramos, A. Maese-Novo, R. Halir, L. Zavargo-Peche, D. Pérez-Galacho, I. Molina-Fernández, J. G. Wangüemert-Pérez, P. Cheben, J. H. Schmid *et al.*, “An ultra-compact multimode interference coupler with a subwavelength grating slot,” *Laser Photonics Rev.* **7**, L12–L15 (2013).
- [23] A. Maese-Novo, R. Halir, S. Romero-García, D. Pérez-Galacho, L. Zavargo-Peche, A. Ortega-Moñux, I. Molina-Fernández, J. Wangüemert-Pérez, and P. Cheben, “Wavelength independent multimode interference coupler,” *Opt. Express* **21**, 7033–7040 (2013).
- [24] R. Halir, I. Molina-Fernández, A. Ortega-Moñux, J. Wangüemert-Pérez, D.-X. Xu, P. Cheben, and S. Janz, “A design procedure for high-performance, rib-waveguide-based multimode interference couplers in silicon-on-insulator,” *J. Lightwave Technol.* **26**, 2928–2936 (2008).
- [25] G. Bouchitte and R. Petit, “Homogenization techniques as applied in the electromagnetic theory of gratings,” *Electromagnetics* **5**, 17–36 (1985).
- [26] Y. Satomura, M. Matsuhara, and N. Kumagai, “Analysis of electromagnetic-wave modes in anisotropic slab waveguide,” *IEEE T. Microw. Theory* **22**, 86–92 (1974).
- [27] “Fimmwave & fimmprop, available from photon design,” <https://www.photond.com>.
- [28] “Fullwave, available from rsoft,” <http://www.rsoftdesign.com>.
- [29] J. G. Wangüemert-Pérez, P. Cheben, A. Ortega-Moñux, C. Alonso-Ramos, D. Pérez-Galacho, R. Halir, Í. Molina-Fernández, D.-X. Xu, and J. H. Schmid, “Evanescent field waveguide sensing with subwavelength grating structures in silicon-on-insulator,” *Opt. Lett.* **39**, 4442–4445 (2014).
- [30] R. Halir, I. Molina-Fernández, J. Wangüemert-Pérez, A. Ortega-Moñux, J. de Oliva-Rubio, and P. Cheben, “Characterization of integrated photonic devices with minimum phase technique,” *Opt. Express* **17**, 8349–8361 (2009).